metals

MDPI

Article

Low-Temperature Impact Fracture Behavior of Medium Manganese Steel with Bcc-fcc Duplex Microstructures

Yu Du [1,2,*], Xiuhua Gao [2,*], Xiaonan Wang [1,*], Hongyan Wu [2], Chao Sun [3], Guosheng Sun [4] and Linxiu Du [2]

[1] School of Iron and Steel, Soochow University, Suzhou 215021, China
[2] State Key Laboratory of Rolling and Automation, Northeastern University, Shenyang 110819, China; wuhy@ral.neu.edu.cn (H.W.); dulx@ral.neu.edu.cn (L.D.)
[3] Nanjing Iron & Steel Co., Ltd., Nanjing 210035, China; sunchao@njsteel.com.cn
[4] Nano and Heterogeneous Materials Center, School of Materials Science and Engineering, Nanjing University of Science and Technology, Nanjing 210094, China; gssun@njust.edu.cn
* Correspondence: duyu2022@suda.edu.cn (Y.D.); gaoxh@ral.neu.edu.cn (X.G.); wxn@suda.edu.cn (X.W.)

Abstract: Impact fracture behavior at low temperatures was investigated in medium manganese steel with bcc-fcc duplex microstructures. The impact energy was above 150 J (−80~20 °C) and the fractography showed dimples for inter-critical annealing at 630 °C (QHA) because of the high retained austenite stability and low martensite dislocation density. The impact energy was from 180 J (20 °C) to 60 J (−80 °C) and the fractography was intergranular for inter-critical annealing at 610 °C (QLA) because of the low stability of RA and carbides precipitated at the prior austenite grain boundaries. The impact energy was below 60 J (−80~20 °C) and the fractography showed cleavage for direct quenching (DQ) because of the high dislocation density of martensite.

Keywords: medium manganese steel; Charpy impact; low-temperature impact fracture behavior; retained austenite

check for updates

Citation: Du, Y.; Gao, X.; Wang, X.; Wu, H.; Sun, C.; Sun, G.; Du, L. Low-Temperature Impact Fracture Behavior of Medium Manganese Steel with Bcc-fcc Duplex Microstructures. *Metals* **2024**, *14*, 293. https://doi.org/10.3390/met14030293

Academic Editor: George A. Pantazopoulos

Received: 1 February 2024
Revised: 25 February 2024
Accepted: 27 February 2024
Published: 29 February 2024

Copyright: © 2024 by the authors. Licensee MDPI, Basel, Switzerland. This article is an open access article distributed under the terms and conditions of the Creative Commons Attribution (CC BY) license (https://creativecommons.org/licenses/by/4.0/).

1. Introduction

For structural steel serving in harsh environments, the impact fracture behavior should be seriously considered [1,2]. Hence, retained austenite (RA) has attracted more and more attention in developing high-strength and high-toughness steels because bcc materials have low-temperature brittleness, while fcc does not [3–5]. Meanwhile, it is widely known that some RA in high-strength steel can significantly increase its toughness and plasticity at the cost of a slight loss of strength [6–8]. Therefore, the effects of RA on the impact fracture of high-strength and high-toughness steels need to be carefully studied and analyzed.

Medium manganese steels with tempered martensite and RA microstructures have attracted significant attention due to their good tradeoff between mechanical properties and material cost [9–11]. Toughness improvement by introducing metastable RA can be maintained when the temperature drops to room temperature [12–14]. Until now, medium manganese steels have been widely used for offshore platforms, which are subjected to low temperatures and high-energy impact loadings, such as typhoons, earthquakes, and tsunamis. Therefore, low-temperature toughness is important for medium manganese steel used for offshore platforms [15–18]. Qi et al. investigated the relationship between the volume fraction and thermal stability of RA in Fe-0.065C-5.45Mn steels at different annealing temperatures of 630 °C, 650 °C, and 670 °C [19]. They found that thermal stability decreases and the volume fraction increases with an increase in annealing temperature. Liao et al. achieved excellent low-temperature impact energy of Fe-0.036C-5.02Mn-1.52Ni in steel through 700 °C inter-critical quenching and inter-critical annealing at different temperatures, where a specimen inter-critically annealed at 590 °C had an impact energy of 133 J when tested at −150 °C [20]. The reason for this good low-temperature impact performance is that RA with high stability provides long-lasting work hardening ability

through continuous deformation-induced transformation during the deformation of steel. These research results indicate that an annealing temperature within a certain narrow range significantly improves the impact energy of medium manganese steels. Exceeding or falling below this narrow temperature range does not achieve the effect of increasing impact energy.

The fundamental cause of low-temperature brittleness is related to the particular screw dislocation core structure and slip behavior of bcc materials [21–23]. The content and stability of RA are achieved by adjusting the annealing temperature, and the martensite's state will also be changed. This change in impact behavior is mainly reflected in the dislocation densities. Researchers mainly focus on the effect of RA on the impact behavior of dual-phase medium manganese steel, but there is little research on the mechanical stability of RA and the deformation coordination between RA and martensite [24,25]. Therefore, it is very important to study the effect of martensite on impact fracture behavior.

This study investigated the impact behaviors of RA and martensite in dual-phase medium manganese steel under different heat treatments. Different inter-critical annealing temperatures obtained specimens with different RA stability and martensite states. The RA volume fractions and the martensite dislocation densities were studied by XRD. The impact energies of different temperatures were obtained by an instrumented impact tester.

2. Experimental Methods

2.1. Materials and Heat Treatment

The tested materials were 30 mm thick Fe-0.065C-0.2Si-5.45Mn medium manganese steel hot-rolled plates. Each plate was hot-rolled from a 230 mm thick industrial continuous casting slab, and there is no macroscopic element segregation in the steel plate. Three kinds of tested steel plates were prepared through different heat treatments to obtain different microstructures. The steel plates were water-quenched to room temperature after being heated to 820 °C for half an hour, which is called DQ. The quenched steels annealed at 630 °C and 610 °C for half an hour are called QHA and QLA, respectively. Different annealing temperatures are used to obtain different RA volume fractions and martensite dislocation densities. Based on the microstructure characterization results in our previous article, the microstructures of DQ only consisted of quenched martensite, while QHA and QLA all consisted of tempered martensite and RA [24,25]. The sizes of prior austenite grain boundaries (GB) of QHA, QLA, and DQ were about 15 μm (Figure 1), and the lath widths of QHA, QLA, and DQ were about 180 nm, 160 nm, and 350 nm (Figure 2), respectively [24,25]. The tensile strength and total elongation of QHA, QLA, and DQ were 725 MPa 26.3%, 795 Mpa 22.5%, and 985 Mpa 15.0%, respectively [24,25].

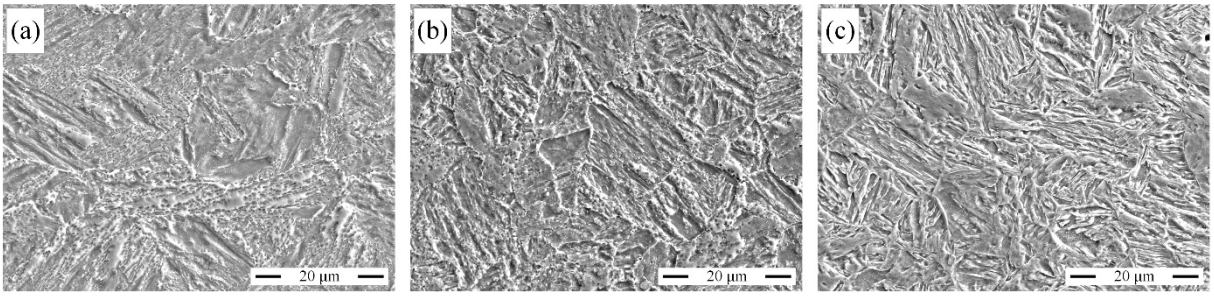


Figure 1. SEM microstructures of different specimens. (**a**) QHA, (**b**) QLA, (**c**) DQ.

2.2. Charpy Impact Test

The impact specimen of 10 × 10 × 55 mm^3 was prepared from one-quarter of the thickness of the steel plate. The specimens were sampled perpendicular to the rolling direction, and the V-notch was along the normal direction. A standard Charpy V-notch impact test at different temperatures was carried out on an MTS ZBC2452-B instrumented pendulum impact tester (450 J) after holding at 20 °C, 0 °C, −20 °C, −40 °C, −60 °C, and

−80 °C for 15 min, where the specimens tested at 20 °C and −40 °C were selected to record a load–displacement curve. Three tests were conducted at each temperature of the three different heat treatment specimens. The fracture morphologies of the specimens tested at 20 °C, −40 °C, and −80 °C were observed by a scanning electron microscope (SEM, Fei-Quanta 600, FEI Company, Hillsboro, OR, USA) at 20 kV. The RA volume fractions in different fracture regions of QHA20 and QLA20 were measured by X-ray diffraction (XRD, SMART LAB 9 kW CuK$_\alpha$, Rigaku Corporation, Tokyo, Japan). The fine microstructures below the fracture surface of QLA−40 and QLA−80 were observed using a field emission transmission electron microscope (TEM, FEI Tecnai G2 F20, FEI Company, Hillsboro, OR, USA). The sampling positions are shown in Figure 3.

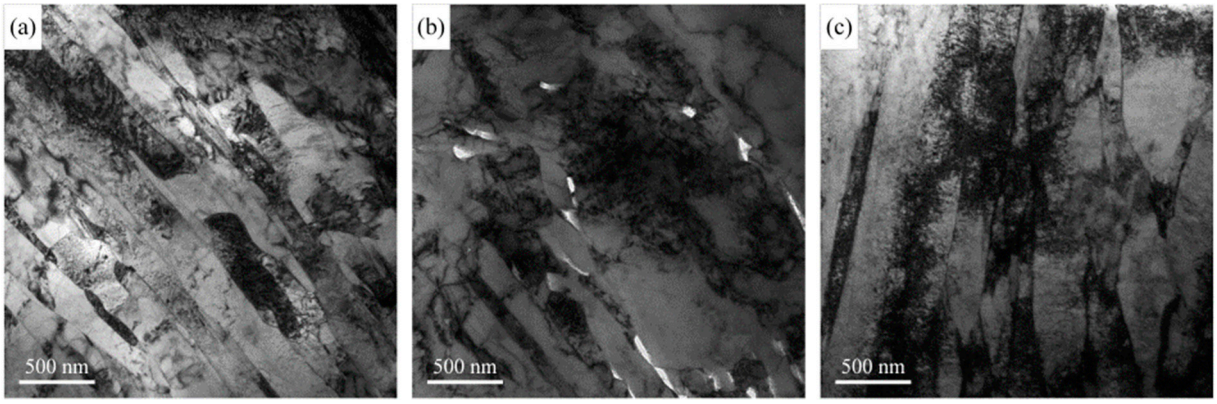


Figure 2. TEM microstructures of different specimens. (**a**) QHA, (**b**) QLA, (**c**) DQ.

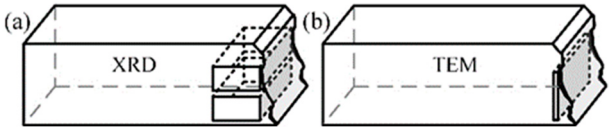


Figure 3. Sketch diagram of sampling positions in impact specimens: (**a**) XRD, (**b**) TEM.

2.3. Microstructure Characterization

An XRD (SMART LAB 9 kW CuK$_\alpha$, Rigaku Corporation, Tokyo, Japan) test was conducted at different isothermal temperatures in the same manner as the impact test. The volume fractions of RA of different specimens after different test temperatures were calculated by Equations (1) and (2) [26,27],

$$V_{\alpha'} + V_\gamma = 1 \tag{1}$$

$$V_\gamma = \frac{1.4I_\gamma}{I_{\alpha'} + 1.4I_\gamma} \tag{2}$$

where $V_{\alpha'}$ and V_γ are the volume fractions of martensite and RA, and $I_{\alpha'}$ and I_γ are the intensities of martensite and RA measured by XRD. The martensite dislocation densities were calculated using (110), (200), (211), (220), and (310). Williamson and Hall suggested that the full width at half-maximum can be evaluated by Equation (3) [28–30],

$$\Delta K = \frac{0.9}{d} + \Delta K^D \tag{3}$$

where ΔK^D represents the line broadening by strain, and d is the average particle size. $\Delta K = 2\delta\cos\theta/\lambda$, and δ, θ, and λ are the full width at half-maximum, the diffraction angle, and the applied X-ray wavelength, respectively. When dislocations cause strain, Equation (3) can be expressed as Equation (4),

$$\frac{2\delta\cos\theta}{\lambda} = \frac{0.9}{d} + \mathrm{Mb}\sqrt{\frac{\pi\rho}{2}}\frac{2\sin\theta}{\lambda}\sqrt{\overline{C}_{h00}\left(1 - q\frac{h^2k^2 + h^2l^2 + k^2l^2}{(h^2 + k^2 + l^2)^2}\right)} \quad (4)$$

where M = 2 is a constant, b = 0.248 nm is the Burgers vector, and $\overline{C}_{h00}$ is 0.285 for pure iron. The value q is the inverse of the intercept on the X-axis in the linear relationship between the left side of Equation (5), and the dislocation density ρ can be calculated.

$$\frac{\left(\frac{2\delta\cos\theta}{\lambda} - \frac{0.9}{d}\right)^2}{\left(\frac{2\sin\theta}{\lambda}\right)^2} = \mathrm{M}^2\mathrm{b}^2\frac{\pi\rho}{2} \times \overline{C}_{h00}\left(1 - q\frac{h^2k^2 + h^2l^2 + k^2l^2}{(h^2 + k^2 + l^2)^2}\right) \quad (5)$$

3. Results

3.1. Microstructure Characterization

The RA volume fraction and martensite dislocation density of the specimens were tested by XRD. The XRD spectrums are shown in Figure 4, and Table 1 lists the RA volume fractions. The RA volume fraction in QHA decreases only slightly with the temperature, whose volume fractions are about 30%. This shows that the thermal stability of RA in QHA is high, and this trend is consistent with the result obtained by Qi et al. [19]. The volume fraction of RA in QLA20 is about 12% and decreases below 5% when the temperature is below 0 °C, and this shows that the thermal stability of RA in QLA is low. As for DQ, there is only a small amount of RA in the specimens at 20 °C, and RA disappears when the isothermal temperature decreases below 0 °C.

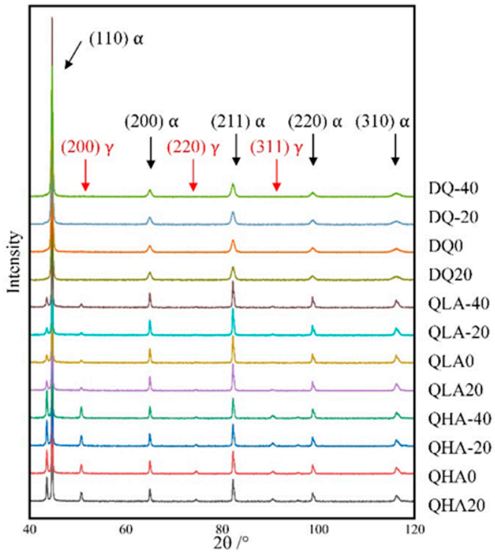


Figure 4. XRD spectrum of the specimens at different isothermal temperatures.

Table 1. RA volume fraction of the specimens at different isothermal temperatures (vol.%).

	−80 °C	−40 °C	0 °C	20 °C
QHA	29.3	30.1	32.1	32.4
QLA	2.6	2.4	4.3	12.3
DQ	0	0	0	1.9

Table 2 lists the martensite dislocation densities of the specimens after holding at different temperatures. The dislocation densities of QHA, QLA, and DQ are 10^{14}, 10^{14}, and 10^{15}, respectively. Additionally, the dislocation density of the specimens annealed at 630 °C

is also lower than that of specimens annealed at 610 °C, because annealing at a higher temperature enables dislocation to recover more completely.

Table 2. The martensite dislocation densities of the specimens after holding at different temperatures ($\times 10^{14}$ m^{-2}).

	−80 °C	−40 °C	0 °C	20 °C
QHA	1.83	1.79	1.69	1.70
QLA	2.25	2.23	2.15	1.92
DQ	18.56	18.02	17.32	17.60

3.2. Charpy Impact Behavior Tested at Different Temperatures

Figure 5 shows the energy–temperature curves of different specimens. The impact energy of QHA20 is about 260 J and of QHA−80 is about 150 J, and QHA did not exhibit a significant ductile–brittle transition. The impact energy of QLA20 is about 190 J and of QLA−80 is about 55 J, and QLA changes from a ductile fracture at 20 °C to a brittle fracture at −40 °C. The impact energy of DQ20 is about 55 J and of DQ−80 is about 10 J.

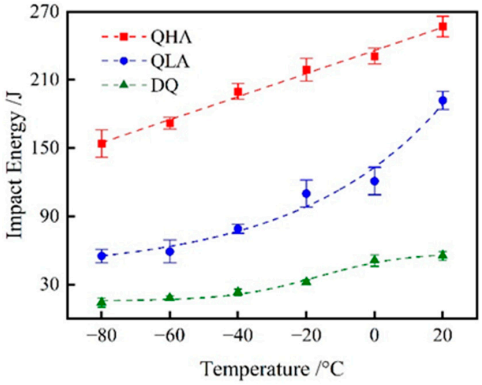


Figure 5. Energy–temperature curves of specimens subjected to different heat treatments.

Figure 6 shows the load–displacement curves of different specimens tested at 20 °C and −40 °C; the points in the picture are displayed at intervals, and the lines are the original output of the machine because the impact equipment denoised the lines. Only DQ−40 is fractured in brittle mode, and the others are fractured in ductile mode. As shown in Figure 6a, all QHA specimens have no unstable crack propagation stage, and the crack formation stages of all QHA specimens are almost the same. It can also be seen that reducing the tested temperature will affect the energy at the later stage of crack propagation. It can be seen from Figure 6b that there is no unstable crack propagation stage in QLA20. However, the unstable crack propagation stage occurs when the test temperature decreases to −40 °C. Figure 6c shows that the curves of DQ20 are composed of crack formation, stable crack propagation, and unstable crack propagation stages. DQ−40 is fractured in the brittle mode because the stress near the notch exceeds the brittle fracture stress of the martensite.

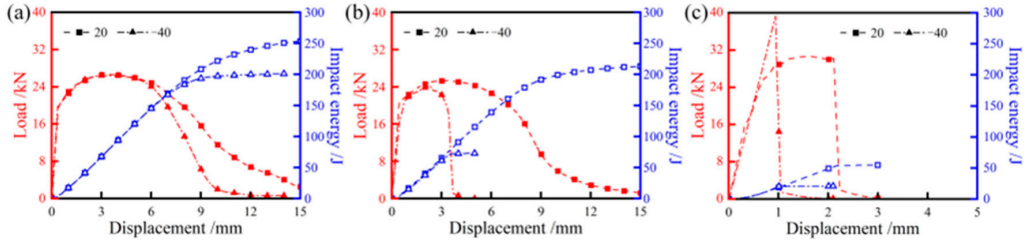


Figure 6. Load–displacement curves of specimens subjected to different heat treatments tested at 20 °C and −40 °C: (**a**) QHA, (**b**) QLA, (**c**) DQ.

3.3. Fractography Observation

The fractography was observed at both macroscopic and microscopic levels for the specimens tested at 20 °C, −40 °C, and −80 °C. Zones A and B of the fracture surface can be considered to be later stage and early stage of crack propagation [31,32]. Figure 7 shows the fractography of QHA tested at 20 °C, −40 °C, and −80 °C. As shown in Figure 7a, Zone A and Zone B are both composed of large and small dimples for QHA20. However, Zone A is composed of small dimples and Zone B is composed of large shallow dimples for QHA−40 (Figure 7b). These indicate that there are impact energy losses throughout the whole stage of crack propagation, which corresponds to the results obtained from the load–displacement curve, as well. But in Figure 7c, the dimple size decreases for Zone A and Zone B. Another apparent phenomenon that can be seen from the macro-fracture is that fracture separation phenomena occurred, and the area of fracture separation increased with the decrease in temperature. This indicates that the fracture mode is not the only factor that affects impact energy, and fracture separation and the corresponding area are also main influences. The notch effect is commonly present in thick specimens, which means there is a transverse force at the notch, which may cause fracture separation. Only the fractography of QHA20 does not experience fracture separation because martensite has strong deformability and is well deformation-coordinated with RA. However, the fractography of QHA−40 and QHA−80 experiences fracture separation because martensite has poor deformation coordination with the new martensite transformed from RA.

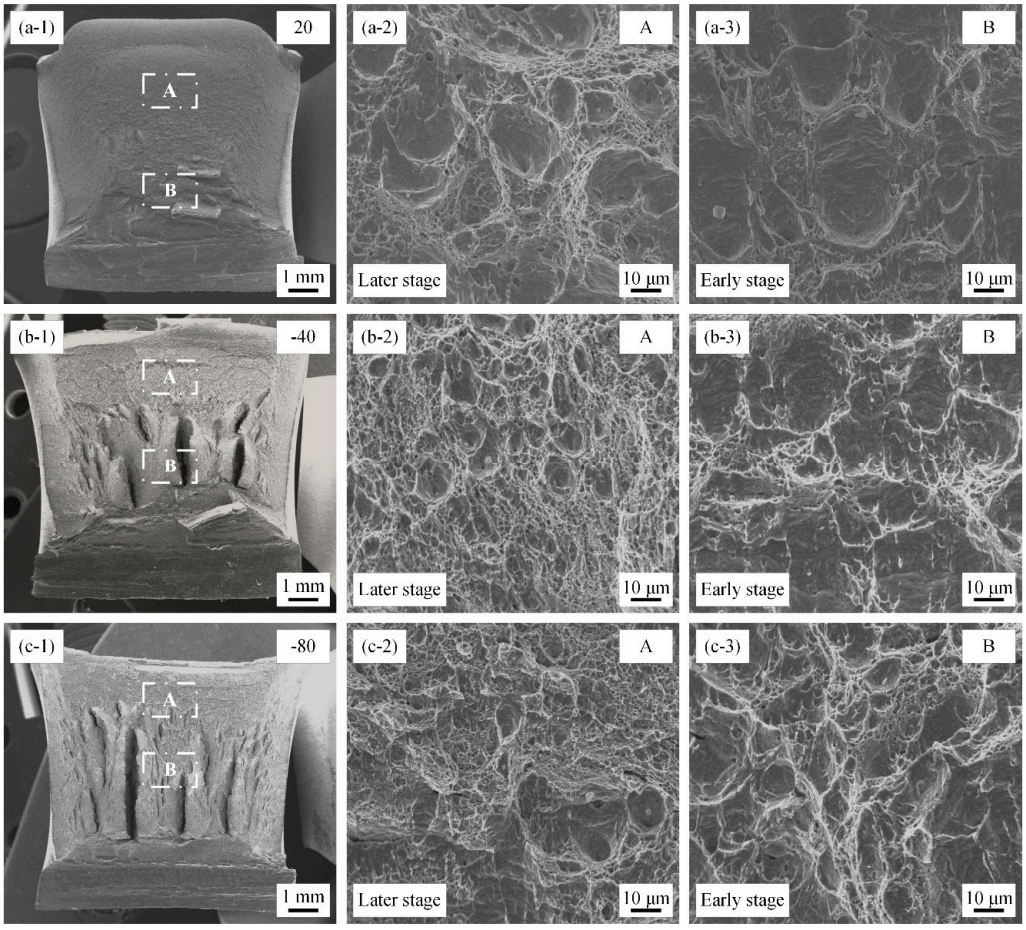


Figure 7. Fractography of QHA specimens tested at different temperatures, and the subfigures 1, 2, and 3 present the macro fractography, the micro fractography of later stage of crack propagation, and the micro fractography of early stage of crack propagation, respectively. (**a**) QHA20, (**b**) QHA−40, (**c**) QHA−80.

Figure 8 shows the fractography of QLA tested at 20 °C, −40 °C, and −80 °C. As shown in Figure 8a, Zone A is composed of small dimples and Zone B is composed of large and small dimples for QLA20. It can be seen in Figure 8b,c that QLA−40 is composed mostly of intergranular and few cleavages, and QLA−80 is composed entirely of intergranular fractures. Some carbides appear on the fracture for both QLA−40 and QLA−80, which shows that the crack propagation stage is fractured in brittle mode after the tested temperature decreases. This may be because the carbide precipitated from the enriched carbon region at the prior austenite GB, reducing the GB binding energy. There is another obvious phenomenon: fracture separation occurs in QLA20 and QLA−40, and the area of fracture separation increases with the decrease in impact energy. The fractography of QLA−80 does not experience fracture separation, because martensite and the new martensite transformed from RA both entered the brittle fracture temperature range with strong deformability and are well deformation-coordinated with RA.

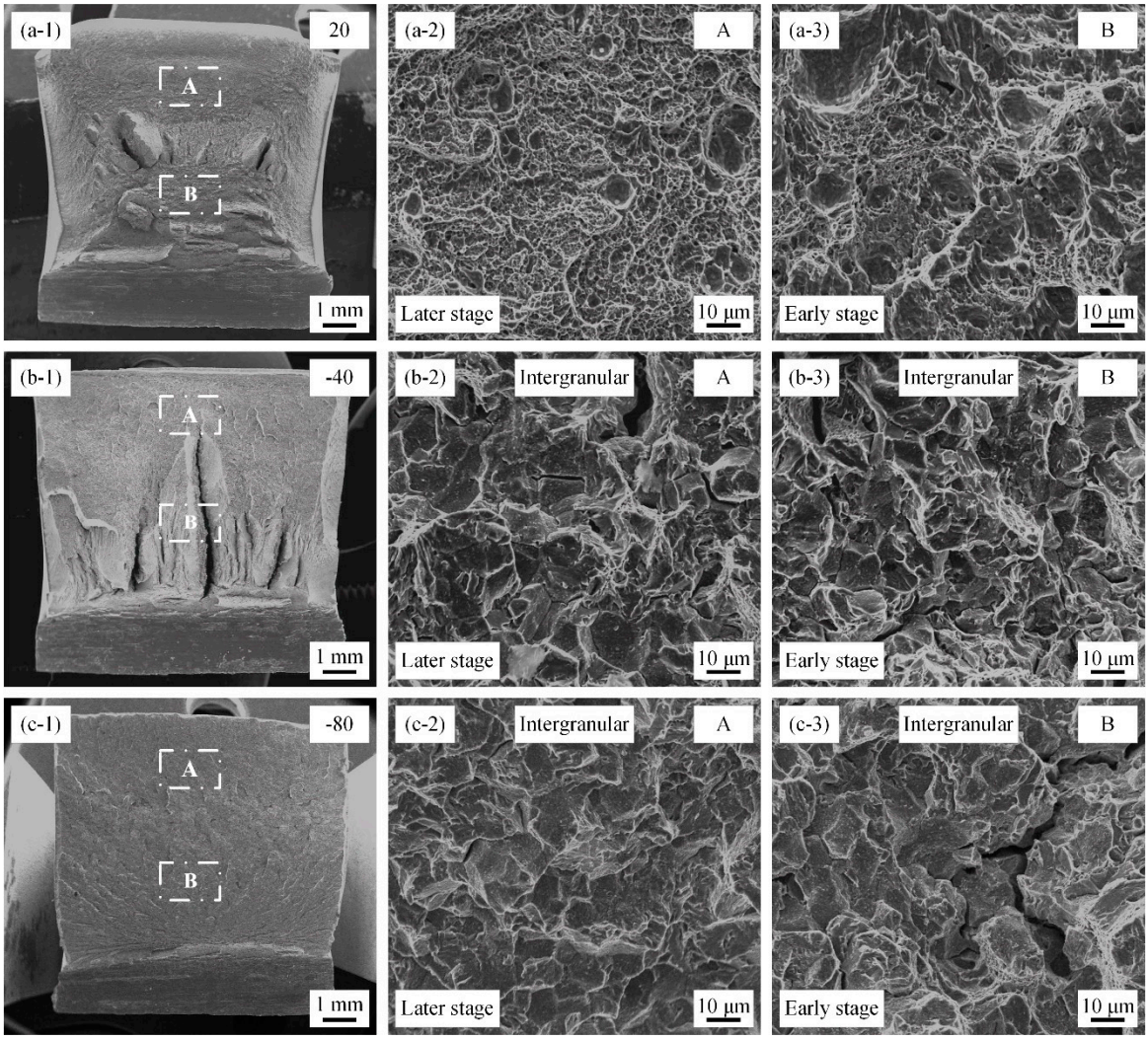


Figure 8. Fractography of QLA specimens tested at different temperatures, and the subfigures 1, 2, and 3 present the macro fractography, the micro fractography of later stage of crack propagation, and the micro fractography of early stage of crack propagation, respectively. (**a**) QLA20, (**b**) QLA−40, (**c**) QLA−80.

Figure 9 shows the fractography of DQ specimens tested at 20 °C, −40 °C, and −80 °C. As shown in Figure 9, only Zone B of DQ20 is composed of small dimples, indicating the impact of toughness losses in the early crack propagation stage. However, all zones of DQ−40 and DQ−80 are composed of cleavage. This shows that the fracture mode of

the early stage of crack propagation changes from ductile to brittle when the temperature decreases to −40 °C and −80 °C.

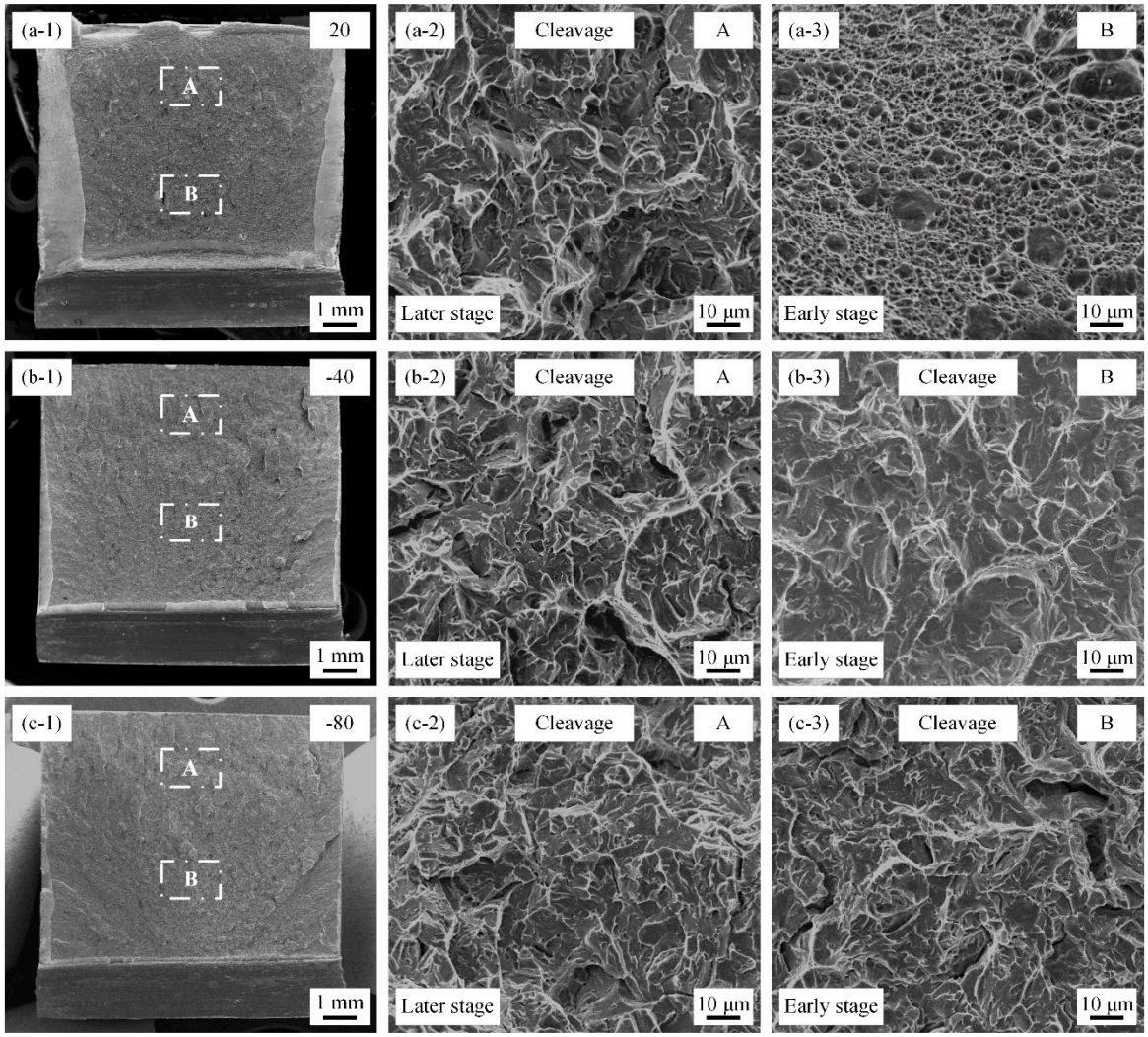


Figure 9. Fractography of DQ specimens tested at different temperatures, and the subfigures 1, 2, and 3 present the macro fractography, the micro fractography of later stage of crack propagation, and the micro fractography of early stage of crack propagation, respectively. (**a**) DQ20, (**b**) DQ−40, (**c**) DQ−80.

Figure 10 shows the XRD spectrums and RA volume fractions of different regions of QHA and QLA tested at 20 °C. The volume fraction of RA in QHA20 is 32.4%, and those of Zone A and Zone B are 2.5% and 12.3%, respectively. This indicates that the plastic deformation at the initial crack propagation stage is less than at the later stage. However, the volume fraction of RA in QLA20 is 12.4%, and those of Zone A and Zone B are 3.1% and 6.7%, respectively. This indicates that the plastic deformation of QLA20 is less than that of QHA20. These results also correspond to the results of the load–displacement curve.

Figure 11 shows TEM microstructures below the fracture surface of QLA−40 and QLA−80. First, compared with macro-fractures, no carbide exists below the fracture surface. This shows that these carbides are only produced during the impact process and only exist on the fracture surface. Because the fracture mode of QLA−40 and QLA−80 is intergranular, the carbides appear at the prior austenite GB. At the same time, corresponding to the TEM picture of QLA at room temperature [24,25], it can be seen that the small amount of RA between martensitic laths disappears after the −80 °C treatment. This means these RA

are transformed into martensite with higher carbon content than the martensite after the −80 °C treatment, and carbides are precipitated under impact load.

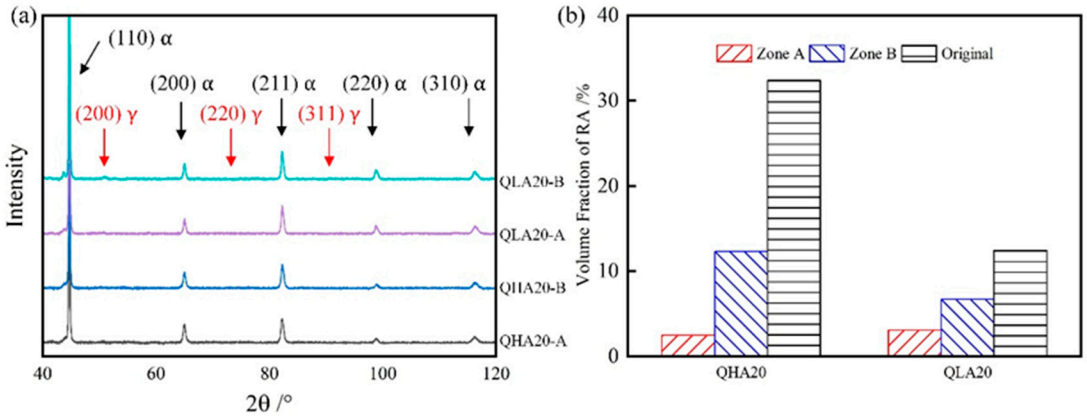


Figure 10. XRD results in different fracture regions: (**a**) XRD spectrum, (**b**) volume fraction of RA.

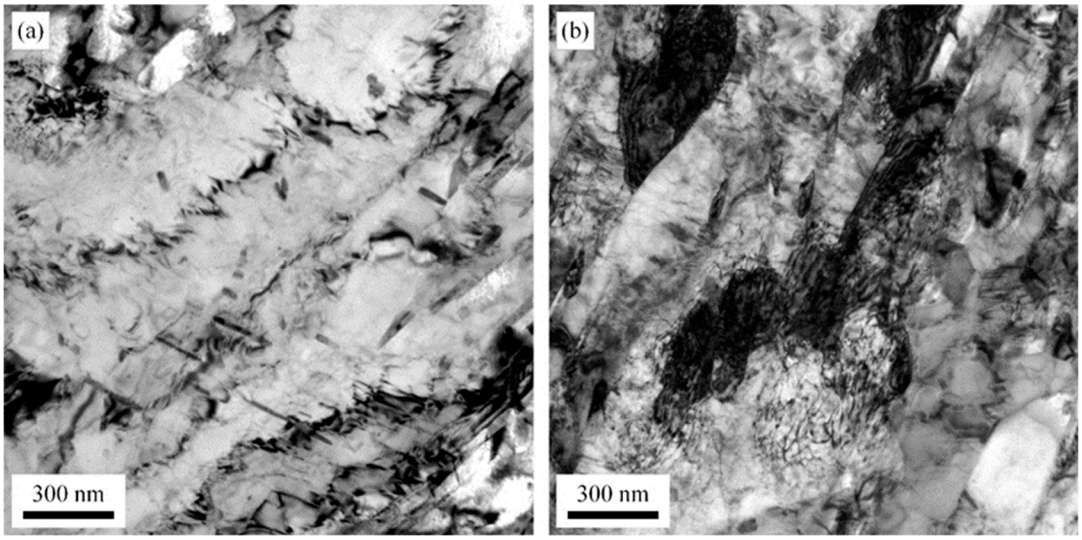


Figure 11. TEM microstructures near the fracture surface: (**a**) QLA−40, (**b**) QLA−80.

4. Discussion

4.1. Low-Temperature Impact Fracture Behavior in Steel of Martensite with RA

The transition from ductile fracture to brittle fracture within a narrow temperature range is called the ductile–brittle transition phenomenon, mainly occurring in bcc materials. The dislocation motion resistance in the lattice increases significantly with the temperature drop because of the small dislocation width. However, materials with an fcc structure dose do not have low-temperature brittleness because of the large dislocation width, which means the yield strength is almost unchanged with temperature drops.

In this paper, the medium manganese steel consists of RA and martensite. The fracture behavior of the specimen is determined by the deformation and fracture behavior of each phase and the stability of RA. The QHA consists of 32.4% RA, which has good thermal stability, with almost no transformation at −80 °C. The impact energy of QHA slowly decreases with decreasing temperature, as shown in the energy–temperature curves (Figure 5), and the fracture surface is entirely composed of dimples. This phenomenon is due to the joint action of tempered martensite with the bcc structure and of RA with the fcc structure. The whole fracture morphology of QHA20 is composed of dimples without fracture separation, which indicates that the deformation capacity of tempered martensite tested at 20 °C under impact load is still very strong, and the main crack propagates along

the direction of the principal stress in the form of micro-void aggregation. Additionally, a fracture separation phenomenon occurs in QHA−40 and QHA−80. According to the general theory of fracture separation formation, the anisotropy of microstructures and the direction of impact are the main factors affecting port separation, especially in steel with an obvious banded microstructure. There are three main reasons for this phenomenon. First is the stress along the thickness direction caused by the deformation constraint, second is the deformation coordination between martensite and RA decreases, and third is the yield strength of martensite increases. It is well known that cleavage cracks are formed mainly due to the stacking of dislocations. However, no cleavage fracture occurred for QHA tested at −40 °C and −80 °C, mainly due to the dislocations in tempered martensite that can slip into RA and avoid dislocation pile-up.

As for QLA, which has a lower volume fraction and stability of RA than QHA, the impact energy of QLA decreases faster than that of QHA with temperature because most RA transforms into martensite after holding at low temperatures (Table 1). The fractography of QLA20 comprises dimples with some fracture separation, because martensite has strong deformability and is well deformation-coordinated with RA. The fractography of QLA−40 is composed of mostly intergranular fractures and few cleavages with more fracture separation, because martensite is poorly deformation-coordinated with the new martensite transformed from RA, resulting in separation under the influence of stress in the thickness direction. However, the fractography of QLA−80 is only composed of intergranular fractures without fracture separation due to the deformability of martensite further decreasing with temperature. It is believed that the strain rate also significantly influences the martensitic transformation of austenite. That is to say, RA's residual content decreases with a deformation degree increase. Thus, it can be inferred that the strain rate is still very large at the early stage of crack propagation, resulting in austenite having no time to transform into martensite. However, the strain rate decreases significantly at the later stage of crack propagation, increasing the amount of austenite transformed into martensite.

It also can be seen from the macro-fracture that some carbides appear on the fracture surface (GB) of QLA−40 and QLA−80, and it is obvious that these carbides exist at the prior austenite GB. The carbide content of QLA−80 is significantly higher than that of QLA−40, which means that lower temperatures can inhibit carbide precipitation. After further TEM observation below the fracture surface (Figure 12), no carbide exists along the lath boundaries below the fracture surface. The carbides along the prior austenite GB are the main reasons for the weakening of GB and the occurrence of intergranular [33,34]. As is well known, for alloy structural steel, there is tempering brittleness during quenching and tempering, which is caused by the carbides precipitated from martensite or the segregation of impurity atoms at the prior austenite GB [35,36]. The specimens annealing at 610 °C and undergoing intergranular fractures at −40 °C and −80 °C were due to the precipitation of carbides at the prior austenite GB. Therefore, the formation of carbides is an important issue that requires careful analysis. There are three possibilities for the occurrence of carbides. First, the phase zone is the ferrite and austenite dual phase zone when the annealing temperature is 630 °C, but the phase zone is closer to the three-phase zone of ferrite, austenite, and cementite when the annealing temperature is 610 °C. When there is local element segregation at the prior austenite GB, there will be carbide precipitation. Second, although there are local elements present, RA is formed, which transforms into martensite and cementite in the low-temperature process. Third, although there are local elements present and RA is formed, it transforms into supersaturated carbon martensite during the low-temperature process. During the impact process, cementite are formed due to the intervention of energy. The main difference between QLA and QHA specimens is that the tempered martensite and RA of QHA−40 and QHA−80 are fractured in ductile mode (dimple), while the martensite of QLA−40 and QLA−80 are fractured in brittle (intergranular) mode fractures. Furthermore, the newly transformed martensite is concentrated near the prior austenite GB. A large amount of carbon is enriched at the prior austenite GB, eventually leading to intergranular fracture.

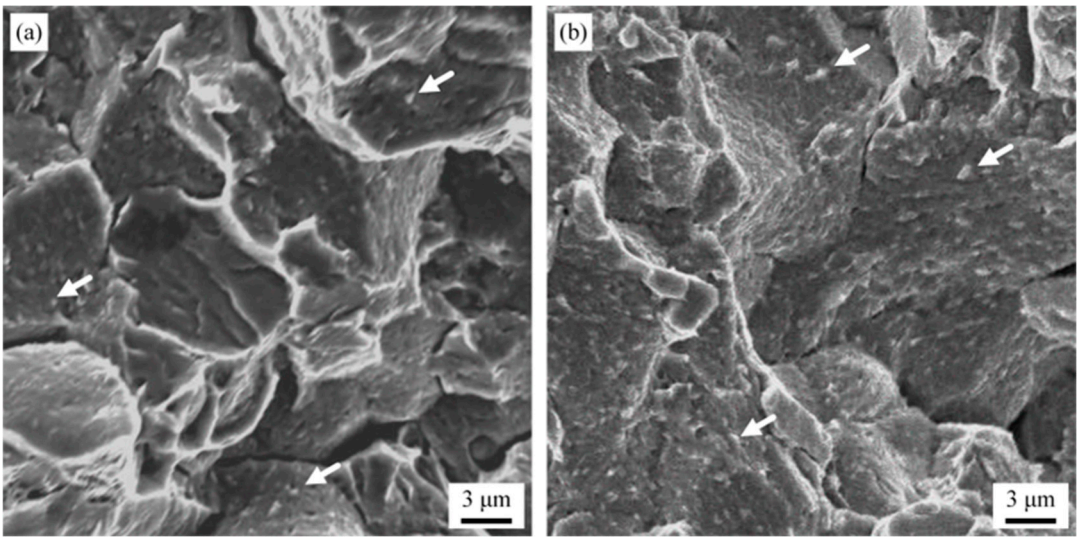


Figure 12. Magnified micro-fractography of QLA−40 and QLA−80: (**a**) QLA−40, (**b**) QLA−80.

4.2. Effect of Dislocation Density of Martensite on Impact Fracture Behavior

In this paper, different microstructures were obtained via three heat treatment processes, including quenched martensite, tempered martensite, and RA. As can be seen from the results of dislocation density, the dislocation density of quenched martensite in DQ20 is about 18.6×10^{14} m^{-2}. However, that of tempered martensite in QHA20 and QLA20 is about 1.8×10^{14} m^{-2} and 2.3×10^{14} m^{-2}, which is one order of magnitude lower than that of quenched martensite. Furthermore, the dislocation density of tempered martensite in QLA20 is higher than in QHA20 because of the low annealing temperature.

As for QHA specimens, carbon atoms segregate at the prior austenite GB, generating RA at the prior austenite GB due to high annealing temperature. Meanwhile, the martensite annealed at 630 °C has higher deformability than that annealed at 610 °C because of the low dislocation density. According to the dislocation pile-up theory, the crack formation of cleavage fracture is caused by dislocation pile-up [37,38]. As a result, the fractures of QHA specimens at all tested temperatures are composed of dimples, which means the plastic deformation capacity is increased during high-temperature annealing. There are two reasons why QHA−80 does not have cleavage fracture: one is that the dislocation density is much lower than that of quenched specimens, although the dislocation density is increased, and the other is that a large amount of stable RA still remains after the −80 °C treatment. On the other hand, QLA specimens have a higher tempered martensite dislocation density and a lower volume fraction of RA with lower stability. QLA−40 and QLA−40 are all composed of intergranular fractures, which indicates that the GB binding force decreases seriously after the tested temperature decreases (carbides).

As for DQ specimens with high dislocation density, DQ20 fractures after yielding because dislocations generate and pile up rapidly during deformation. However, DQ−40 shows a complete brittle fracture mode, fractured at the elastic stage, because yield stress and dislocation density increase rapidly with the decrease in temperature [39,40]. Furthermore, the significant lattice distortion in quenched martensite also increases the resistance of dislocation movement, thus reducing the ability of plastic deformation. Therefore, when the tested temperature drops to −40 °C, the plastic deformation disappears and consists entirely of cleavage fracture. There is no intergranular fracture because there is no carbon segregation at the prior austenite GB, which means no GB weakening.

5. Conclusions

This study used an impact test to study the low-temperature impact behavior of QHA, QLA, and DQ specimens. The low-temperature impact fracture was analyzed through

fracture morphology, RA volume fraction, and the martensite dislocation density. We obtained the following conclusions:

(1) The impact energy of QHA decreases slowly with temperature through the joint action of the bcc and fcc microstructures. The fracture morphology of QHA is entirely composed of dimples because of the low dislocation density of the martensite and the large volume fraction of RA with high stability.
(2) The impact energy of QLA decreases faster than that of QLA with temperature, and QLA is fractured in intergranular mode, while the tested temperature decreases below −40 °C because of the low stability of RA and carbides precipitated at the prior austenite grain boundaries.
(3) The impact energy of DQ tested at different temperatures is low and fractured in the elastic stage when the tested temperature is below −40 °C. DQ−40 and DQ−80 are fractured in cleavage mode instead of intergranular because of the high dislocation density in quenched martensite.

Author Contributions: Conceptualization, Y.D., X.G. and L.D.; methodology, H.W.; validation, X.W., C.S. and G.S.; formal analysis, X.G. and L.D.; investigation, H.W., C.S. and G.S.; writing—original draft preparation, Y.D.; writing—review and editing, X.G. and X.W.; visualization, H.W., C.S. and G.S.; supervision, L.D.; project administration, X.G., X.W. and L.D.; funding acquisition, X.W. and L.D. All authors have read and agreed to the published version of the manuscript.

Funding: The authors gratefully appreciate the financial support from the National Natural Science Foundation of China (No. 51975391) and the National High-tech R&D Program (863 Program) [NO. 2015AA03A501].

Data Availability Statement: The original contributions presented in the study are included in the article, further inquiries can be directed to the corresponding author/s.

Conflicts of Interest: The Author C.S. was employed by the Nanjing Iron and Steel Co., Ltd. The remaining authors declare that the research was conducted in the absence of any commercial or financial relationships that could be construed as potential conflicts of interest. The funders had no role in the design of the study; in the collection, analyses, or interpretation of data; in the writing of the manuscript; or in the decision to publish the results.

References

1. Dadfarnia, M.; Novak, P.; Ahn, D.C.; Liu, J.B.; Sofronis, P.; Johnson, D.D.; Robertson, I.M. Recent Advances in the Study of Structural Materials Compatibility with Hydrogen. *Adv. Mater.* **2010**, *22*, 1128–1135. [CrossRef]
2. Zhao, J.X.; Wang, H.; Koenigsmann, K.; Ran, X.Z.; Zhang, P.; Zhang, S.Y.; Li, Y.; Liu, H.; Liu, H.; Ren, L.; et al. Warm Deformation at the ($\alpha + \gamma$) Dual-Phase Region to Fabricate 2 GPa Ultrafine-Grained TRIP Steels. *Metals* **2023**, *13*, 1997. [CrossRef]
3. Yang, J.L.; Huang, F.; Guo, Z.H.; Rong, Y.H.; Chen, N.L. Effect of retained austenite on the hydrogen embrittlement of a medium carbon quenching and partitioning steel with refined microstructure. *Mater. Sci. Eng. A* **2016**, *665*, 76–85. [CrossRef]
4. Chen, L.; Ma, Z.X.; Shi, R.J.; Su, Y.J.; Qiao, L.J.; Wang, L.L. Comprehensive effect of hydrostatic compressive stress in retained austenite on mechanical properties and hydrogen embrittlement of martensitic steels. *Int. J. Hydrogen Energy* **2020**, *45*, 22102–22112. [CrossRef]
5. Zhang, Y.D.; Hui, W.J.; Zhao, X.L.; Wang, C.Y.; Cao, W.Q.; Dong, H. Effect of reverted austenite fraction on hydrogen embrittlement of TRIP-aided medium Mn steel (0.1C-5Mn). *Eng. Fail. Anal.* **2019**, *97*, 605–616. [CrossRef]
6. Zhao, J.; Jiang, Z. Thermomechanical processing of advanced high strength steels. *Prog. Mater. Sci.* **2018**, *94*, 174–242. [CrossRef]
7. Dong, Y.; Zhang, B.; Zhao, M.M.; Du, Y.; Misra, R.D.K.; Du, L.X. Investigation of austenite decomposition behavior and relationship to mechanical properties in continuously cooled medium-Mn steel. *Mater. Sci. Eng. A* **2022**, *831*, 142208. [CrossRef]
8. Cho, L.; Kong, Y.R.; Speer, J.G.; Findley, K.O. Review: Hydrogen Embrittlement of Medium Mn Steels. *Metals* **2021**, *11*, 358. [CrossRef]
9. Scott, C.P. Recent Developments in Medium and High Manganese Steels. *Metals* **2022**, *12*, 743. [CrossRef]
10. Sun, B.H.; Lu, W.J.; Gault, B.; Ding, R.; Makineni, S.K.; Wan, D.; Wu, C.H.; Chen, H.; Ponge, D.; Raabe, D. Chemical heterogeneity enhances hydrogen resistance in high-strength steels. *Nat. Mater.* **2021**, *20*, eaay1430. [CrossRef]
11. Saha, D.C.; Biro, E.; Gerlich, A.P.; Zhou, Y. Influences of blocky retained austenite on the heat-affected zone softening of dual-phase steels. *Mater. Lett.* **2020**, *264*, 127368. [CrossRef]
12. Cai, Z.H.; Ding, H.; Misra, R.D.K.; Ying, Z.Y. Austenite stability and deformation behavior in a cold-rolled transformation-induced plasticity steel with medium manganese content. *Acta Mater.* **2015**, *84*, 229–236. [CrossRef]

13. Lan, L.Y.; Yu, M.; Qiu, C.L. On the local mechanical properties of isothermally transformed bainite in low carbon steel. *Mater. Sci. Eng. A* **2019**, *742*, 442–450. [CrossRef]
14. Huang, L.; Liu, J.; Deng, X.T.; Wang, Z.D. Achieving High Plasticity and High Toughness of Low-Carbon Low-Alloy Steel through Intercritical Heat Treatment. *Metals* **2023**, *13*, 1737. [CrossRef]
15. Dulucheanu, C.; Severin, T.L.; Cerlinca, D.A.; Irimescu, L. Structures and Mechanical Properties of Some Dual-Phase Steels with Low Manganese Content. *Metals* **2022**, *12*, 189. [CrossRef]
16. Zou, Y.; Xu, Y.B.; Hu, Z.P.; Gu, X.L.; Peng, F.; Tan, X.D.; Chen, S.Q.; Han, D.H.; Misra, R.D.K.; Wang, G.D. Austenite stability and its effect on the toughness of a high strength ultra-low carbon medium manganese steel plate. *Mater. Sci. Eng. A* **2016**, *675*, 153–163. [CrossRef]
17. Zou, Y.; Xu, Y.B.; Hu, Z.P.; Chen, S.Q.; Han, D.T.; Misra, R.D.K.; Wang, G.Z. High strength-toughness combination of a low-carbon medium-manganese steel plate with laminated microstructure and retained austenite. *Mater. Sci. Eng. A* **2017**, *707*, 270–279. [CrossRef]
18. Chen, J.; Zhang, W.N.; Liu, Z.Y.; Wang, G.D. The role of retained austenite on the mechanical properties of a low carbon 3Mn-1.5Ni steel. *Metall. Mater. Trans. A* **2017**, *48*, 5849–5859. [CrossRef]
19. Qi, X.Y.; Du, L.X.; Hu, J.; Misra, R.D.K. Effect of austenite stability on toughness, ductility and work-hardening of medium-Mn steel. *Mater. Sci. Tech. A* **2019**, *35*, 2134–2142. [CrossRef]
20. Liao, Z.H.; Dong, Y.; Du, Y.; Wang, X.N.; Qi, M.; Wu, H.Y.; Gao, X.H.; Gao, L.X. Effects of different intercritical annealing processes on microstructure and cryogenic toughness of newly designed medium-Mn and low-Ni steel. *J. Mater. Res. Technol.* **2023**, *23*, 1471–1486. [CrossRef]
21. Duesbery, M.S.; Vitek, V. Plastic anisotropy in b.c.c. transition metals. *Acta Mater.* **1988**, *46*, 1481–1492. [CrossRef]
22. Vitek, V. Core structure of screw dislocations in body-centred cubicmetals: Relation to symmetry and interatomic bonding. *Philos. Mag.* **2004**, *84*, 415–428. [CrossRef]
23. Mrovec, M.; Gröger, R.; Bailey, A.G.; Nguyen-Manh, D.; Elsässer, C.; Vitek, V. Bond-order potential forsimulations of extended defects in tungsten. *Phys. Rev. B* **2007**, *75*, 104119. [CrossRef]
24. Du, Y.; Gao, X.H.; Lan, L.Y.; Qi, X.Y.; Wu, H.Y.; Du, L.X.; Misra, R.D.K. Hydrogen embrittlement behavior of high strength low carbon medium manganese steel under different heat treatments. *Int. J. Hydrogen Energy* **2019**, *44*, 32292–32306. [CrossRef]
25. Du, Y.; Gao, X.H.; Du, Z.W.; Lan, L.Y.; Misra, R.D.K.; Wu, H.Y.; Du, L.X. Hydrogen diffusivity in different microstructural components in martensite matrix with retained austenite. *Int. J. Hydrogen Energy* **2021**, *46*, 8269–8284. [CrossRef]
26. Fan, Y.H.; Zhang, B.; Yi, H.L.; Hao, G.S.; Sun, Y.Y.; Wang, J.Q.; Han, E.H.; Ke, W. The role of reversed austenite in hydrogen embrittlement fracture of S41500 martensitic stainless steel. *Acta. Mater.* **2017**, *139*, 188–195. [CrossRef]
27. Lee, Y.K.; Han, J. Current opinion in medium manganese steel. *Mater. Sci. Technol.* **2015**, *31*, 843–856. [CrossRef]
28. Takebayashi, S.; Kunieda, T.; Yoshinaga, N.; Ushioda, K.; Ogata, S. Comparison of the dislocation density in martensitic steels evaluated by some x-ray diffraction methods. *ISIJ Int.* **2010**, *50*, 875–882. [CrossRef]
29. Yin, F.; Hanamura, T.; Umezawa, O.; Nagai, K. Phosphorus-induced dislocation structure variation in the warm-rolled ultrafine-grained low-carbon steels. *Mater. Sci. Eng. A* **2003**, *354*, 31–39. [CrossRef]
30. Ungár, T.; Dragomir, I.; Révész, Á.; Borbély, A. The contrast factors of dislocations in cubic crystals the dislocation model of strain anisotropy in practice. *J. Appl. Crystal.* **1999**, *32*, 992–1002. [CrossRef]
31. Kryzhanivskyy, Y.; Poberezhny, L.; Maruschak, P.; Lyakh, M.; Slobodyan, V.; Zapukhliak, V. Influence of test temperature on impact toughness of X70 pipe steel welds. *Procedia Struct. Integr.* **2019**, *16*, 237–244. [CrossRef]
32. Jiang, J.; Wu, M.; Xu, T.T.; Bao, W.; Li, Z.H. Study on impact toughness of TMCP and quenched and tempered high strength steels. *Case Stud.* **2024**, *20*, e02795. [CrossRef]
33. Kokawa, H.; Shimada, M.; Sato, Y.S. Grain-boundary structure and precipitation in sensitized austenitic stainless steel. *JOM* **2000**, *52*, 34–37. [CrossRef]
34. Tomotaka, H.; Kota, S.; Kaoru, S.; Kazuhiro, K. Beneficial role of the grain boundary precipitates for intergranular creep fracture of 25Cr–20Ni–Nb–N steel. *Mater. Sci. Eng. A* **2023**, *882*, 145487.
35. Zabil'skii, V.V. Temper embrittlement of structural alloy steels (review). *Met. Sci. Heat Treat.* **1987**, *29*, 32–42. [CrossRef]
36. Capus, J.M. *Temper Embrittlement in Steel*; Newhouse, D.L., Ed.; ASTM International: West Conshohocken, PA, USA, 1968.
37. Michot, G. Mechanical analysis of the interaction between a semi-infinite Griffith crack and its coplanar plastic zone. *Eur. J. Mech. A-Solid* **2023**, *100*, 104982. [CrossRef]
38. Zhang, J.D.; Sheng, Y.; Yang, H.D.; Wu, J.B.; Jiang, X.Y. Influence of Dislocation Pile-Up on Main Crack Propagation in Nanocrystals in the Hydrogen Environment. *Acta Mech. Solida Sin.* **2023**, *36*, 851–859. [CrossRef]
39. Zhu, J.; Barber, G.; Sun, X.C. Effects of Isothermal Temperature on Dislocation Density in Bainite Transformation of 4140 Steel. *Materials* **2022**, *15*, 6066. [CrossRef]
40. Jiang, C.P.; Ma, H.C.; Chen, Y.N.; Wang, N.; Zhao, Q.Y.; Wu, G.; Zhu, L.X.; Luo, J.H.; Zhao, Y.Q. Crack propagation behavior of dual-phase steel at low temperature. *Int. J. Fatigue* **2022**, *155*, 106633. [CrossRef]

Disclaimer/Publisher's Note: The statements, opinions and data contained in all publications are solely those of the individual author(s) and contributor(s) and not of MDPI and/or the editor(s). MDPI and/or the editor(s) disclaim responsibility for any injury to people or property resulting from any ideas, methods, instructions or products referred to in the content.